Assembly Level Modeling and Transportation Damage Prediction of Used Nuclear Fuel (UNF) Cladding – 14569

Scott Sanborn *, Brian Koeppel *, Nicholas Klymyshyn *, Harold Adkins *, Kenneth Geelhood *
* Pacific Northwest National Laboratory, Richland, WA

ABSTRACT

Under U.S. Nuclear Regulatory Commission (NRC) regulations, UNF must maintain its integrity in such a way that it can withstand the physical forces of handling and transportation associated with restaging the fuel and moving it to a different location such as an interim storage site, a geologic repository, or a treatment/recycling facility. Hence, understanding mechanical performance under cumulative loading stemming from normal conditions of storage (NCS), transfer from storage container to transport container if needed, and normal conditions of transport (NCT) is necessary as it establishes part of the safety basis via maintaining the fuel confining boundary (geometry), maintaining criticality safety, and is one of the critical components to the preservation of retrievability. An initial demonstration of modeling and simulation capabilities was performed as part of a collaborative effort between Pacific Northwest National Laboratory (PNNL), Sandia National Laboratories (SNL), Idaho National Laboratory (INL), Oak Ridge National Laboratory (ORNL), and the Transportation Technology Center Inc. (TTCI). This demonstration completed preliminary deterministic evaluations of moderate-to-high burnup UNF mechanical performance under NCS and NCT conditions. This paper focuses on work performed by PNNL on the assembly level modeling of a UNF assembly and fuel cladding damage predictions under NCT loads. The Finite Element (FE) model created for a 17 x 17 Pressurized Water Reactor (PWR) optimized fuel assembly (OFA) is discussed along with the communications to and from the fuel rod-level and cask-level models. Additionally, the methodology for determining cumulative damage is discussed including the 3000 mile damage prediction from a 10 second simulation. The damage results are shown for five shock and vibration broadened loading histories. It is found that predicted cladding strains were not large enough to cause structural failure, but cyclic strains roughly projected for the entire route were significant in some cases. The total damage from summation of the worst shock and vibration cases evaluated is approximately 18% of the expected fatigue limit. Therefore it is predicted that the fuel rods do not fail during NCT given the assumptions used throughout this initial demonstration.

INTRODUCTION

The implementation of consolidated interim storage of UNF, consistent with one of the Blue Ribbon Commission on America's Nuclear Future recommendations [1] and DOE's recently published *Strategy for the Management and Disposal of Used Nuclear Fuel and High-Level Radioactive Waste* [2] would necessitate the implementation of a large-scale transportation program. Some of the used fuel in the inventory may be transported at least twice to get it to a repository—once from the reactor spent fuel pool to the consolidated interim storage facility and then to a repository for final disposal—after an unknown storage duration. Given the uncertainty in material properties of high burnup UNF, variability in storage duration, and the potential variability in the magnitude and duration of normal loading during transport, it is appropriate to investigate whether or not single or multiple transports would have a negative impact on fuel integrity and its suitability to meet the regulations regarding retrievability after transport. Hence,

understanding performance characteristics of UNF cladding and ancillary components under cumulative loading stemming from NCS, transfer (from storage container to transport container if needed), and NCT is necessary. This understanding establishes the safety basis by maintaining the fuel confining boundary (geometry), maintaining criticality safety, and is one of the critical components to the preservation of retrievability.

With this background in mind, work was done to demonstrate that enough information, experimental support, and modeling and simulation capabilities exist to establish a preliminary determination of UNF structural performance under NCT loading. To demonstrate this capability a multilevel sub-modeling approach was used consisting of three levels of sub-models: cask, assembly, and fuel rod (see Fig. 1). Additionally, material properties, component temperatures, and fuel post-irradiation conditions were needed as inputs to this approach. Each level utilized finite element analysis sub-modeling techniques to accurately model the complete spent nuclear fuel transport system on the railcar (cask restraint structure, cask, basket, and fuel). These three modeling levels required some two-way information exchange between each other. Finally, the modeling outputs were fuel rod stresses and strains for failure prediction. For complete details on the entire initial demonstration, including a number of sensitivity studies, see Adkins et al. [3]. An overall summary of this entire approach is presented by Geelhood et al. [4]. Details of the cask-level modeling [5], fuel rod/grid-level modeling [6, 7], and associated fatigue testing [8] are available in accompanying papers. This paper focuses on the assembly level modeling efforts and fuel cladding damage predictions for this demonstration.

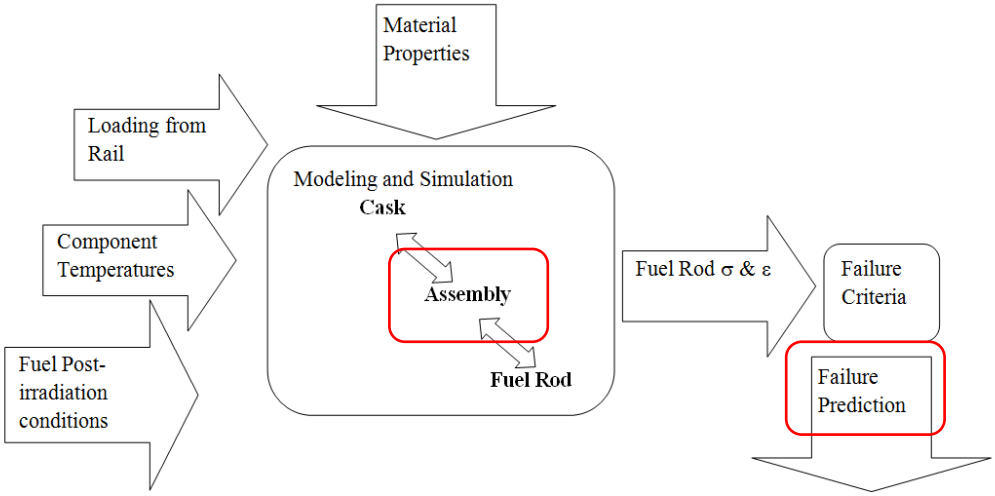

Fig. 1. Schematic overview of modeling approach.

The assembly sub-model uses accelerations from the cask sub-model as input loadings; for conservatism the input accelerations enveloping all of the basket cells from the cask-level model [5] were enveloped and broadened based on the expected uncertainty and variations in the cladding properties to ensure that the greatest fuel rod response was induced (details of this process can be found in Adkins et al. [3]). The assembly sub-model also uses fuel material properties and grid leaf spring/dimple behaviors from the single fuel rod-level model [6] as inputs. The objective of the assembly-level sub-model is to determine the stress and strain states in all of the fuel rods within a single assembly during the transportation loading shock and vibration events. This information is used to assess the damage of the cladding during a typical 3000 mile rail trip.

To assess the cladding damage, a methodology has been developed to analyze the potential for failure for the shock loads separately from the vibrational loads. Due to the significant required computational time for these FE models, only a 10 second window (of either a shock event or characteristic vibrational loading) of a 3000 mile trip is analyzed. Because of this, a conservative methodology is developed to predict the damage over the entire trip from just the 10 second window results. A Rainflow counting algorithm [9] is used to calculate the number and amplitude of cladding strain cycles for the 10 second window. The strain cycle history is then used with experimental fatigue data and a Miner's rule linear damage approach to compute a cumulative fatigue damage fraction over the 3000 mile trip. While the initial demonstration, presented in Adkins et al. [3], included damage results for a number of sensitivity studies and initial, final, and final broadened loading inputs, the damage results shown here are presented for the best estimate material properties under final broadened transportation loadings.

ASSEMBLY LEVEL MODEL DESCRIPTION

The PWR assembly model is a three-dimensional LS-DYNA®[a] explicit transient FE model of a single full Westinghouse Electric (WE) 17×17 Optimized Fuel Assembly (OFA). The model includes geometric representations of the major structural components in a full single assembly including the upper nozzle/tie plate, lower nozzle/tie plate, guide/measurement tubes, spacer grids, and fuel rods (Fig. 2) as well as the basket walls and spacer blocks that surround the assembly in the cask (Fig. 3). Additionally, the inclusion of a control head assembly was also considered since such activated hardware may be transported simultaneously with the assembly and adds additional mass that may influence the dynamic response. This assembly sub-model is used to estimate the stresses and strains on the fuel rod cladding during transient dynamic shock and vibration events that occur under NCT.

Fig. 2. Overall WE 17×17 OFA PWR fuel assembly sub-model (w/o control components, spacer blocks, or basket).

The following are the major assumptions and simplifications made in the assembly sub-model:

[a] LS-DYNA is a registered trademark of Livermore Software Technology Corporation in the United States and/or other countries.

- The fuel rod (fuel pellets, cladding, plenum spring, thimbles, etc.) was modeled as a solid beam with effective bending stiffness, mass and damping properties.
- The spacer grid slots were modeled as a simplified box structure, and spacer grid leaf springs/dimples were modeled as translational springs.
- Leaf springs and dimples were assumed to be fully relaxed due to in-core creep; i.e. there was no preload remaining in the springs or dimples.
- The basket was modeled as a rectangular enclosure and assumed rigid during transient dynamic events.
- Only the end plates of the spacer blocks were modeled as part of the basket enclosure.
- Temperature fields for mechanical property assignment were assumed constant with four axial zones along the assembly.
- Friction coefficients of 0.2 static and 0.1 dynamic were assumed; these relatively low values conservatively allow for more translation of the assembly inside the basket.
- Cladding strains at the outer diameter of the fuel rods were the primary result of interest.
- Thermal strains were not considered.
- Intermediate flow mixers were neglected because they were assumed to be completely deteriorated and not present.

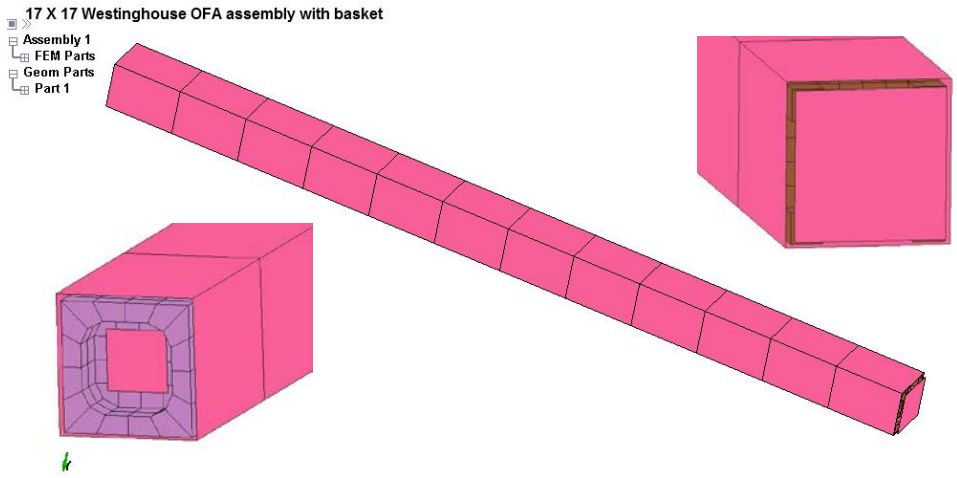

Fig. 3. Compartment walls and spacer block end plates forming the basket enclosure for the assembly sub-model.

Model Geometry and Mesh

The geometry of the WE 17×17 OFA assembly was taken primarily from the physical descriptions and dimensions provided in the available public documents [10, 11] to construct the FE model (for more details see Adkins et al. [3]). Simplified geometries were used for the upper nozzle/tie plate, bottom nozzle/tie plate, and control head assembly to eliminate unnecessary geometric details. These simplified structures retained the proper mass and acceptable inertial properties, so they are not expected to have significantly different interactions with the other components. The assembly was then supported within a box structure representative of a single basket compartment. This structure consisted of a rectangular box with open ends to represent the basket side walls, and the same initial gap sizes used in the cask model between

the assembly and basket were maintained. Only the end plate surfaces of each spacer block nearest the assembly were modeled.

The model mesh of most of the assembly sub-model is shown in Fig. 4. The fuel rods and guide tubes were meshed with 2-node Hughes-Liu beam elements with a solid circular cross section for the fuel rods and a thin wall tube for the guide tubes (these solid beam elements have the same effective cross-sectional properties and density as cladding encased used fuel as determined from the rod-level analyses [6]). The spacer grids were meshed with 4-node reduced integration Belytschko-Tsay shell elements. The complex geometric details of the numerous possible spacer grid, leaf spring, dimple, and flow diverter configurations were not modeled. Rather the rods were laterally supported by two orthogonal sets of translational springs in every slot (each vertical and horizontal set consisted of one leaf spring at the geometric center of the slot and two opposing dimples separated by a distance of 46 mm) as shown in Fig. 5. Guide tubes were rigidly connected to the corresponding slots in the spacer grids via the LS-DYNA® "spotweld" connection such that bending moments were properly transferred. The top and bottom tie plates were modeled with 8-node constant stress brick elements. The tie plates were similarly connected with the guide tubes to transfer bending moments (Fig. 6). For models with the control head assembly, a single large diameter beam was connected via smaller diameter beams to the 24 guide/measurement tube locations of the top nozzle (Fig. 7). This transferred the moment of the cantilevered head assembly mass to the guide tubes and upper tie plate, but any consideration of control head axial sliding within the guide tubes was neglected. The basket and spacer block plates surrounding the assembly were meshed with shells as shown in Fig. 3.

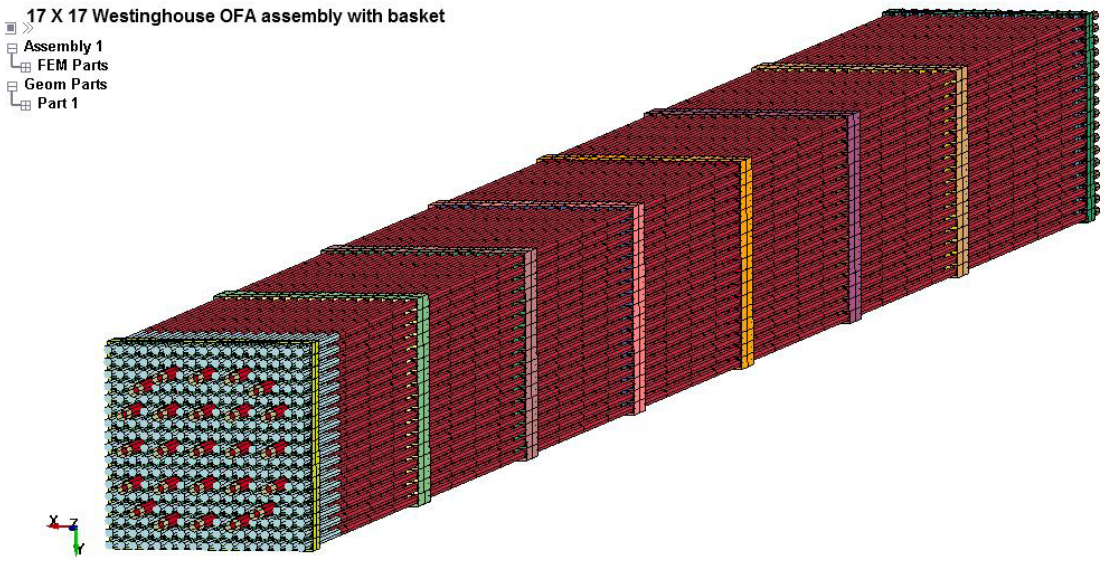

Fig. 4. WE 17×17 OFA PWR fuel assembly sub-model (end tie plates/nozzles removed)

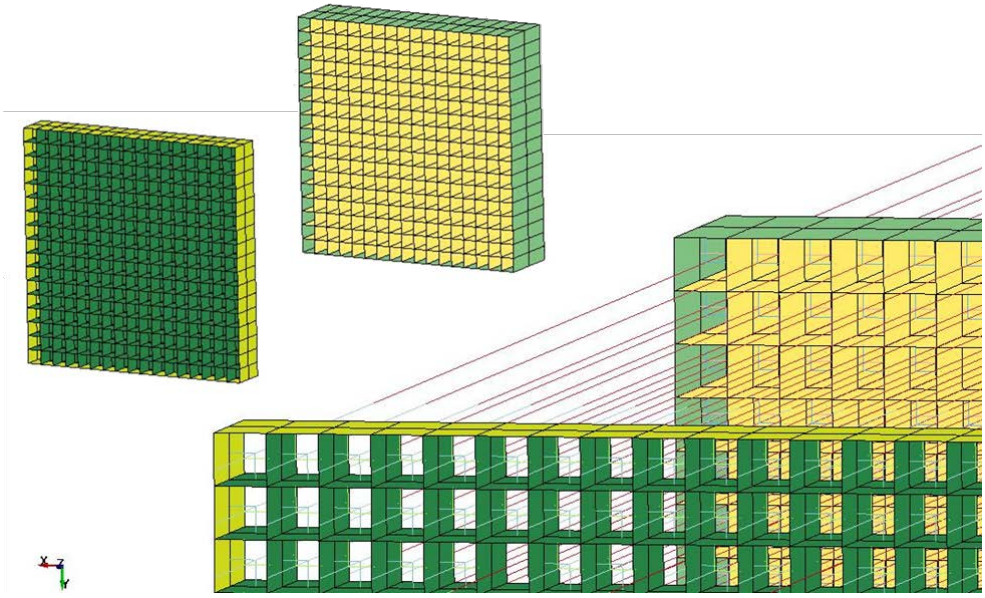

Fig. 5. End Inconel and middle Zircaloy spacer grids with fuel rods (beam elements are represented as lines) supported by spring elements representing the two leaf springs and four dimples within each slot.

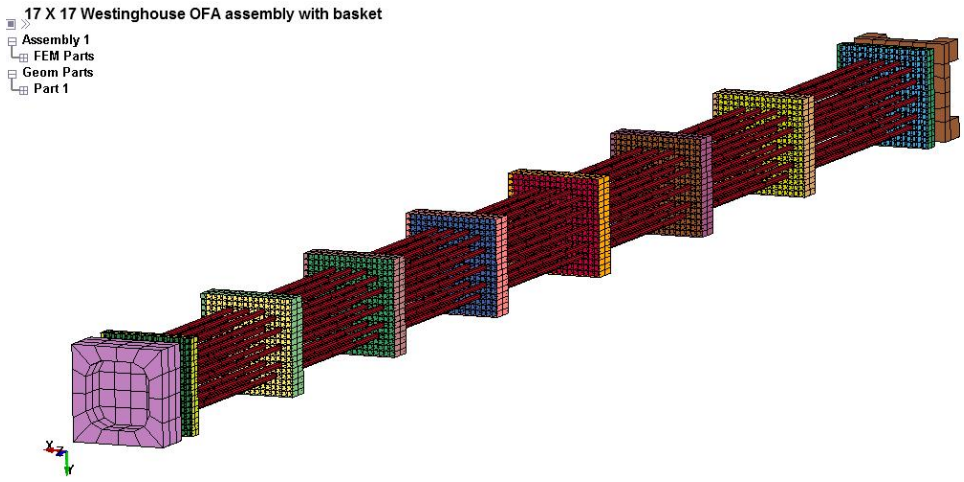

Fig. 6. Assembly support skeleton consisting of the guide tubes, spacer grids, lower tie plate/nozzle, and upper tie plate/nozzle.

Explicit FE calculations require that the model integration time step be smaller than the shortest duration for stress wave propagation through an element (Courant-Friedrichs-Levy stability criterion). To maximize the permissible time step and reduce the total solution time, elements with small dimensions were eliminated from the model as much as possible. Alternatively, mass can also be judiciously added to small elements to increase the density and reduce the local wave propagation speed, but the added mass must be small relative to the actual mass of the structure so as to not significantly affect the overall dynamic response. In anticipation of long

solution times, special care was taken in model meshing to maximize the time step. In particular, the spacer grids were meshed as only two elements per side of each slot and the geometry of the tie plates/nozzles was also modified to eliminate small elements. These modifications resulted in a model with a permissible time step of 2.1×10^{-6} seconds. The mesh of the various components is shown in Fig. 2 through Fig. 7. Overall, the model consisted of approximately 140,000 nodes and 60,000 elements.

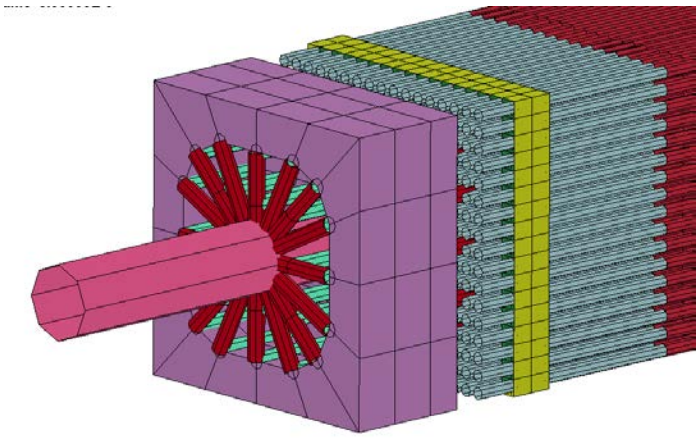

Fig. 7. Simplified beam element control head assembly added to the top tie plate/nozzle and connected to the control rods/guide tubes.

Contact between interacting components was implemented in several locations. General surface-to-surface contact with friction was defined between the grids and tie plates of the assembly and the basket walls. A beam-to-surface contact definition included the fuel rods to capture potential contact between the rods and basket during lateral vibration. Node-to-surface contact with friction was defined between the spacer block end plates and the tie plates/nozzles and/or control head assembly. Tied node-to-surface contact was assigned between the spacer grid and the springs representing the leaf springs and dimples. This method was chosen over using common nodes to permit spring placement at their actual locations on the spacer grid independent of the local grid mesh density (which was necessarily coarsened to increase the time step). Finally, the guide tubes were attached to the spacer grids using rigid constraints via the generalized spot weld option.

Loads, Boundary Conditions, and Solution Procedure

A gravitational body load of 9.807 m/s^2 was applied to all components during both the initialization and the transient dynamic phases of the model solution. A uniform temperature load was applied to four regions along the assembly length for assignment of temperature-dependent material properties. For the results shown here, temperatures were representative of an assembly at the center of the cask with temperatures of 550.1, 632.6, 641.4, and 608.7 K defined across 4 axial regions. Material properties used in the model are not discussed here but can be found in Adkins et al. [3].

The solution procedure for the assembly model included an initialization step to establish contact due to gravity followed by a transient dynamic calculation. During the initialization step,

the gravitational body load was imposed on the model and the assembly came to rest on the floor of the basket. This step induced the initial strain in the fuel rod cladding due to sagging of the rods between the grid supports. During the model initialization stage, the basket walls were constrained while the assembly was allowed to establish contact with the basket floor due to gravitational loading. The transient dynamic calculation was then initiated with application of the loading time-histories. During the transient excitation, acceleration time-histories from the cask-level analysis were applied to the basket and spacer block plates. For the basket compartment side walls and spacer block plates, a rigid body was generated between all basket nodes and a node at the basket centroid. Rotational and translational accelerations from the cask-level model for the centroid of a specific basket compartment were applied to the center rigid body node which then appropriately transfers the rigid body translations and rotations to all of the nodes on the basket and spacer block plate boundaries. Further details on the model input history data is provided in Adkins et al. [3]. Cladding strains in all of the rods were output for post-processing and subsequent use in the failure analysis effort.

Communications To and From Rod-Level and Cask-Level Models

The assembly-level sub-model received inputs from both the rod-level [6] and cask-level [5] models. Based on the rod-level analyses, data regarding the fuel rod bending stiffness, fuel rod Raleigh damping parameters due to possible pellet-clad interactions, spacer grid leaf spring stiffness, spacer grid dimple stiffness, and cladding tensile bending stress concentration due to pellet-pellet gaps were utilized. The cask-level analyses consisted of five independent shock or vibration events, each consisting of 10 seconds of simulated time. Due to practical constraints on total computational time, these 10 seconds of simulated time were extracted for the worst events occurring in longer railcar loading time histories; as discussed later conservative assumptions were made to apply the model results to a 3000 mile rail route. For each of these five independent events, the six degree-of-freedom motion (axial, lateral, and vertical translational and rotational accelerations) was obtained for the entire basket. Based on the basket compartment of interest, the appropriate acceleration histories provide the time-dependent accelerations representing the selected shock or vibration excitation. Acceleration time-histories were additionally processed via filtering to eliminate high frequency numerical noise generated in the cask-level model output accelerations. Furthermore, bounding cases with broadened response curves that fully encompass the responses of all 32 individual basket compartments were generated to ensure maximum rod excitation for a final conservative evaluation of each loading condition (see Adkins et al. [3] for more details). This final broadened acceleration input was used to conservatively predict the amount of cladding damage for the fuel rods.

A surrogate fuel assembly model was used to represent an individual assembly in the cask-level model. The surrogate model was defined to sufficiently represent the mass, stiffness, and inertial properties of the individual fuel assembly to capture the fundamental modes of its dynamic response. An approach of using a coarsely-meshed continuum representation of the assembly with effective properties was utilized. Solid mechanics calculations for beam and plate bending were used to estimate effective orthotropic normal and shear moduli for the simplified assembly. Effective densities were calculated based on the surrogate volume. Modal analysis of the surrogate assembly was then performed and the results were compared to modal results of the full detailed assembly. The comparison of the mass, inertia, and modal properties between the two models is discussed in more detail in Adkins et al. [3]. The

surrogate model was deemed sufficiently representative of the detailed model based on the reasonable matching of these properties. This surrogate model was used for an approximate representation of all 32 assemblies in the cask-level model [5, 3].

The assembly sub-model predicted the stresses, strains, total axial force, and total bending moment of the effective fuel rod elements for the simulated loading duration. From this data history, the peak cladding strain or stress was identified for failure analysis of an overloading condition. This data history was also used to determine the cyclic strain history for the loading duration using Rainflow counting procedures [9]. Therefore, the model results were analyzed to determine the cladding peak strain and cyclic strain history.

Since the fuel rods were represented as solid circular beams with an equivalent effective bending stiffness E×I (modulus multiplied by area moment of inertia) to model actual cladding with used fuel in them, additional steps are needed to get the cladding strain from the model. For each fuel rod beam element in the model, the resultant axial force and the two resultant bending moments about the local element axes were tabulated for each loading history. Using this unfiltered data, the elastic axial strain and bending strains were computed at four locations on the outer surface of the cladding (Fig. 8) according to Eq. 1 below where E is the elastic modulus, F_{axial} is the resultant axial force, r is the clad outer radius, $K_{tension}$ is the tensile stress concentration factor, and M_{bend1} and M_{bend2} are the resultant local beam bending moments.

$$\varepsilon_1 = \frac{1}{E}\left(\frac{F_{axial}}{\pi r^2} + K_{tension}\left(\frac{M_{bend1} r}{\frac{\pi}{4} r^4}\right)\right)$$

$$\varepsilon_2 = \frac{1}{E}\left(\frac{F_{axial}}{\pi r^2} + K_{tension}\left(\frac{M_{bend2} r}{\frac{\pi}{4} r^4}\right)\right) \qquad \text{(Eq. 1)}$$

$$\varepsilon_3 = \frac{1}{E}\left(\frac{F_{axial}}{\pi r^2} - \left(\frac{M_{bend1} r}{\frac{\pi}{4} r^4}\right)\right)$$

$$\varepsilon_4 = \frac{1}{E}\left(\frac{F_{axial}}{\pi r^2} - \left(\frac{M_{bend2} r}{\frac{\pi}{4} r^4}\right)\right)$$

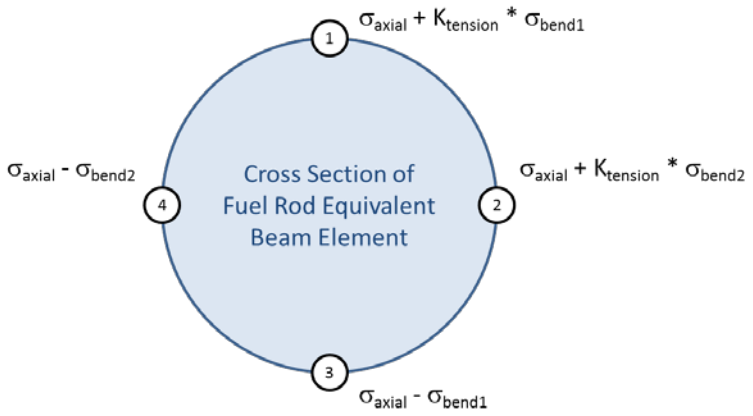

Fig. 8. Calculation locations of beam cladding strains.

Tensile bending strains were multiplied by a stress concentration factor of 1.38 based on analysis of a detailed rod with fuel pellets [6]. This analysis showed that the local tensile

bending stress in the cladding was higher than the compressive bending stress because the individual fuel pellets can support a compressive load but likely do not carry tension at the pellet-pellet interface. The tensile bending stress concentration was also supported by an independent fuel rod analysis [7]. Therefore cladding on the tensile side during fuel rod bending must carry more of the load, and this effect was conservatively included in the strain history calculations. At each of these locations on the rods, Rainflow counting procedures [9] were used to compute the amplitudes and total number of strain cycles experienced by the cladding. The fatigue limit curves presented in Adkins et al. [3] were used to determine the fatigue damage at each location, and the location with the highest damage was selected for extension to a 3000 mile rail route. The histogram of strain cycle amplitudes at the worst rod location for the 10 second simulation window was output for a prediction of total damage under the entire transport route.

FAILURE APPLICATION

The cladding stress and strain history predicted by the detailed assembly model (informed by the rod-level and cask-level models under rail-related NCT conditions) was used to estimate cladding integrity. The cladding stress and strain history was broken down into shock events and vibrational loading.

Failure Application Methodology

For shock events, the maximum predicted cladding strain was compared to predicted uniform elongation at the appropriate conditions. For vibrational loading, the strain history was broken up into various cyclic strain magnitudes and the calculated number of occurrences. Because there will be a different number of cyclic strains at different magnitudes, a damage fraction was calculated that includes the cyclic loadings at various amplitudes. This approach known as the Rainflow-counting algorithm is often used to calculate failure due to fatigue and counting methods are established in ASTM E 1049-85 [9]. The Rainflow algorithm is a useful method to obtain a set of strain reversal cycles of various amplitudes from a complex time history. To calculate the fatigue damage fraction, the vibrational loading history was binned into a number of strain amplitudes and the number of cycles at each of these amplitudes was tabulated. For each strain amplitude, the fatigue strength, S, was calculated according to:

$$S = \frac{1}{2} E \varepsilon_T \qquad \text{(Eq. 2)}$$

Where S is the fatigue strength, E is the elastic modulus, and ε_T is total strain change over the cycle.

For each fatigue strength calculated, the fatigue-design curve (developed in Adkins et al. [3] and shown later as a solid black line in Fig. 11) was used to determine the allowable number of cycles at that strain amplitude (a damage fraction was calculated by dividing the anticipated number of cycles at that strain amplitude by the number allowed at that amplitude). The cumulative damage fraction was calculated by adding the individual damage fractions for each strain amplitude to the damage fraction from each shock loading event according to:

$$DamageFraction = \sum_{i=1}^{n} \frac{N_i}{\left(N_{allow}\right)_i} + \sum_{j=1}^{m} \frac{\left(\varepsilon_{plastic}\right)_j}{UE_j} \qquad \text{(Eq. 3)}$$

where N_i is the number of anticipated cycles at a given strain amplitude, N_{allow} is the number of allowable cycles at a given strain amplitude, $\varepsilon_{plastic}$ is the plastic strain from a given shock loading event, and UE is the uniform elongation for a given shock loading event. The methodology described above to analyze the potential for failure from shock and vibration is shown graphically in Fig. 9. Note: the modeling results indicated that the maximum loads were significantly less than the yield stress (i.e. no plastic strain was observed) which made the second portion of Eq. 3 unnecessary.

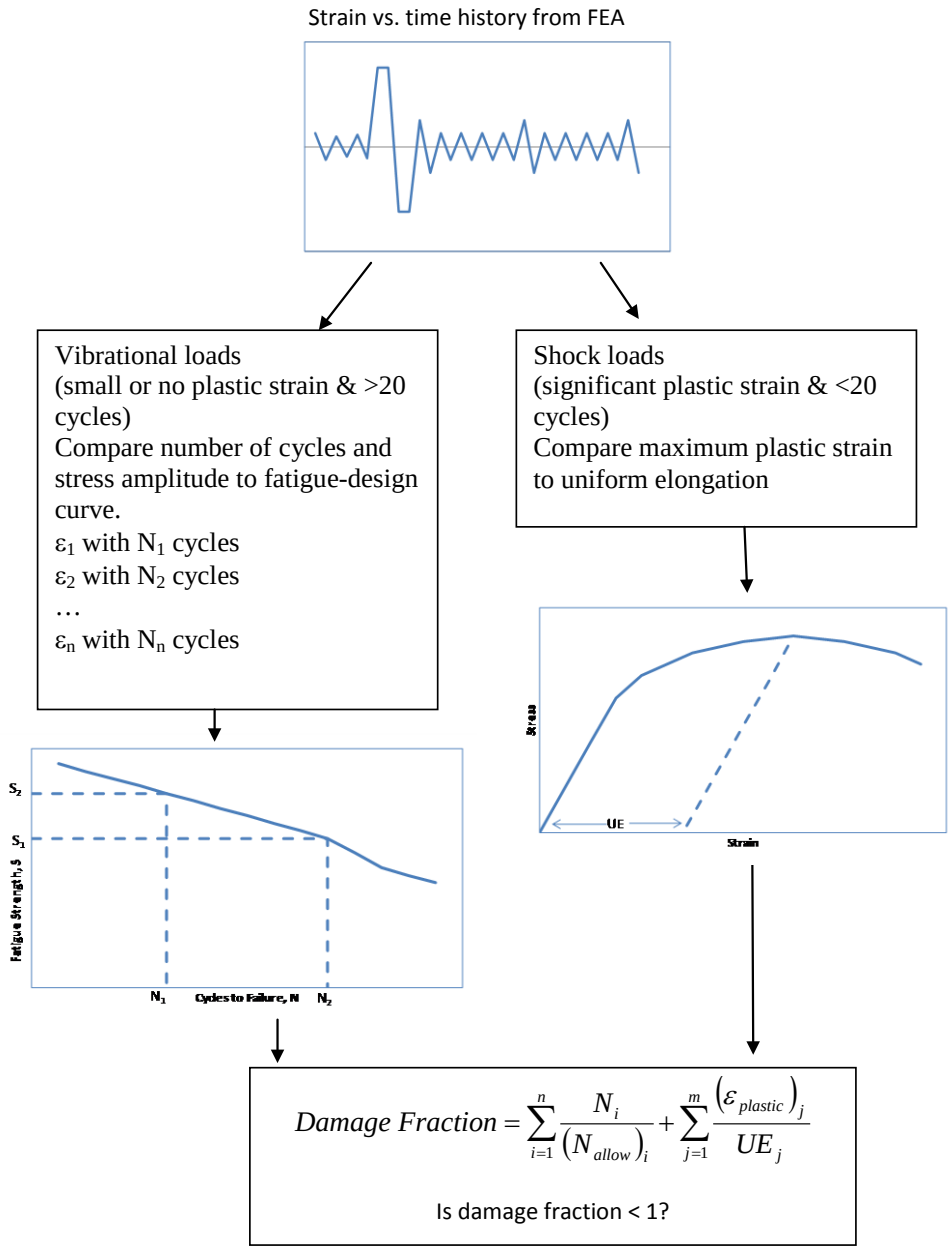

Fig. 9. Methodology to analyze the potential for failure for the shock loads and vibrational loads.

If the comparisons of the cladding stress and strain history to these failure criteria show that the fuel assembly performance during NCT is significantly below the established failure criteria, then this may provide adequate demonstration that the cladding will not experience gross failure. If the resulting FEM stress/strain history indicates conditions that are close to the established failure criteria, then further experimental work may be required to refine the current failure curves.

Extension to 3000 Mile Rail Route

To extend the 10 second results to the entire 3000 mile rail route, two separate approaches were used for vibration and shock. With the vibrational loads it is assumed that the amplitude of vibration is linear with rail speed and the measured strain in the rods is proportional to the amplitude. Based on the 10 second window and the expected duration at different railcar velocities during the 3000 mile trip, partial damage distributions for the expected trip velocity spectrum (given in Adkins [3]) are calculated. It is assumed that the damage is linear such that individual damage contributions from different strain amplitudes can be added together. The partial damage contributions at each speed are then summed to determine the total vibrational damage to the fuel cladding over the 3000 mile route.

The shock run damage ratio is calculated by reviewing the vertical cask-level input shock time history and determining the approximate number of unique shock events in a small representative time history (350 seconds). The number of total shock cycles for the 3000 mile trip is then calculated by using the time of rail transport for the entire trip. The occurrence frequency and cyclic amplitude for the shock events is assumed to be independent of rail speed, but the cyclic strains are scaled by the different amplitudes of the 10 shock events in the 350 second window evaluated. For more details on the vibration and shock methods to extend the results to the 3000 mile route see Adkins et al. [3]. The damage ratio from the bounding shock event is then added to the bounding damage ratio for the vibration event to produce the total damage fraction.

Cladding Damage Results

The 10 second acceleration inputs (that were enveloped and broaden for conservatism) were applied to the detailed assembly level FE model discussed earlier for five shock and vibration cases. This loading was significant enough to cause lateral and axial sliding of the assembly within the basket and impact with the side walls, but the assembly did not separate from the basket floor due to vertical loading. Significant amplification of the assembly response was observed for all cases at frequencies above 40 Hz consistent with the estimated rod natural frequencies of 50-60 Hz (see Adkins et al. [3]).

From the simulation, the local strains along the fuel rod cladding were calculated according to the previous section. Next, the cumulative shock and vibration damages over the 10 second simulation were determined using the Rainflow algorithm. Finally, the worst damage locations were extended from the 10 second window to the entire 3000 mile rail route using the methods described above. Fig. 10 shows the maximum cladding strain (left) and total fatigue damage (right) for the broadened shock and vibration cases. TABLE I summarizes the maximum cladding strain, the maximum cyclic strain amplitude, and the total fatigue damage (over 3000 miles) for each of these five loading cases. The predicted cladding strains were not large

enough to cause structural failure. However, the cumulative loading is enough to cause some significant cyclic fatigue damage. The maximum total fatigue damage is approximately 7% for the shock cases and approximately 11% for the vibration cases. In both cases the lateral loading events resulted in the highest damage. Fatigue damage projections for the vertical shock was 5% while the vertical and longitudinal vibration cases were less than 1%. Considering the total damage as the summation of the worst shock and vibration cases approximately 18% of the expected fatigue limit for the cladding is reached.

TABLE I: Total Cladding Fatigue Damage Due to Broadened Loading.

Load Case	Maximum Cladding Strain	Maximum Cyclic Strain Amplitude	Total Fatigue Damage
Lateral Shock	7.52×10^{-4}	1.02×10^{-3}	7.34%
Vertical/Longitudinal Shock	6.41×10^{-4}	9.54×10^{-4}	4.57%
Lateral Vibration	5.55×10^{-4}	9.30×10^{-4}	11.04%
Vertical Vibration	3.84×10^{-4}	5.04×10^{-4}	0.34%
Longitudinal Vibration	3.82×10^{-4}	5.72×10^{-4}	0.37%

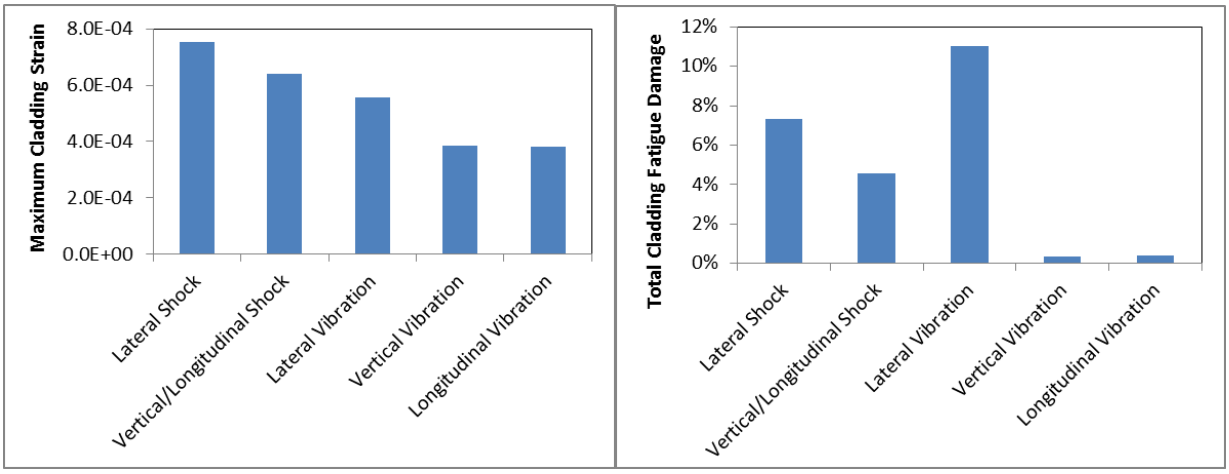

Fig. 10. Comparison of maximum cladding strain (left) and total fatigue damage (right) for broadened shock and vibration cases.

Alternatively, the damage results can be visually compared to the fatigue design curve developed in Adkins et al. [3] by assuming all cycles occur at the maximum cyclic strain amplitude and thus a corresponding stress level can be calculated. Fig. 11 shows a comparison of the damage for these five cases against the fatigue design curve. Also shown in Fig. 11 is the experimental data used to develop this fatigue design curve. Much of the data in Fig. 11 is obtained for higher stress levels, uses specimen geometries other than tubes, and is primarily for unirradiated Zircaloy. Additional fatigue data on representative bending geometries of irradiated materials would be extremely valuable in ensuring the true fatigue limit of the high burn-up cladding material state has been adequately quantified.

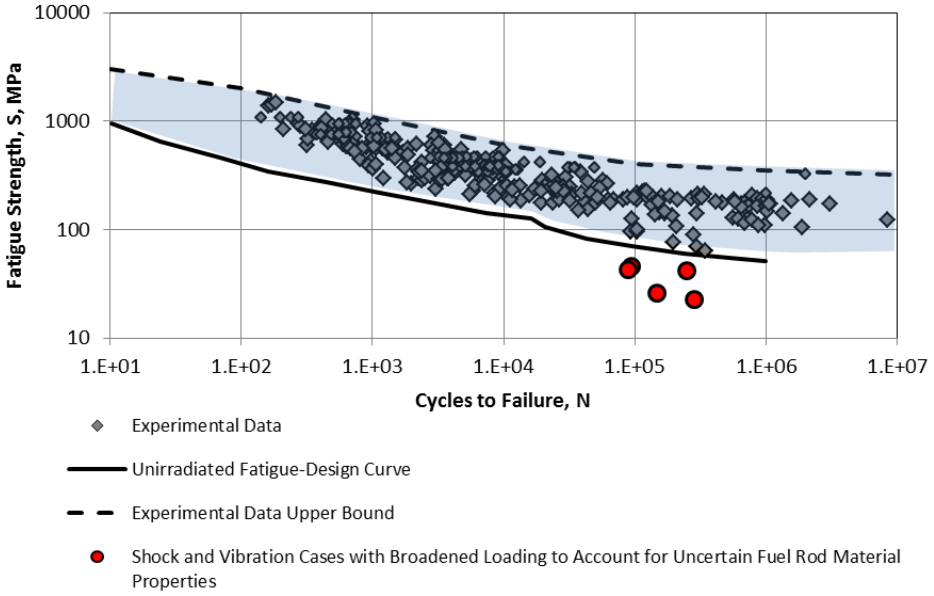

Fig. 11. Clad fatigue damage summary for shock and vibration cases with broadened loading.

CONCLUSIONS

A detailed model of the WE 17x17 OFA PWR assembly was constructed in LS-DYNA®. Transient dynamic cases were run with input loading that bounded the response of all 32 basket compartments and peak broadened to account for uncertainty in the fuel rod properties after storage. The lateral shock case exhibited the highest cladding strain in the transient dynamic model, but the lateral vibration case had the highest potential fatigue damage.

The predicted cladding strains were not large enough to cause structural failure (i.e. no plastic strain occurred under any loading), but cyclic strains projected for the entire route were significant in some cases. A Rainflow counting procedure was used to compute the magnitude and number of cladding strain cycles for each fuel rod element in the assembly. These strain cycles are binned and counted for the 10 second simulation time and then extrapolated for a 3000 mile trip. The total damage was then computed by summing the contributions from each of the strain bins. For the enveloped and broadened loading, cumulative fatigue damage for the lateral vibration case was projected to be 11% of the critical value based on the representative 10 second window response. The cumulative fatigue damage for the lateral shock case was 7% for a conservative accounting of frequent high amplitude shock events over the entire route. Therefore, considering that the total damage from summation of the worst shock and vibration cases is approximately 18% of the expected fatigue limit, the fuel rod cladding does not fail during NCT given the assumptions listed.

It is important to note this work is only part of an initial demonstration [3] in which reasonable assumptions were made. There are a number of important variables warranting further investigation that may alter the conclusions of this work including (but not limited to): spacer grid influence (ORNL bend fixture modification and testing); influence of vacuum drying mechanisms; coupled influence of cladding material and burnup; influence of packaging configuration; shaker tests of an assembly simulating rail related frequencies and

displacements; collection of prototypic UNF rail conveyance data; and consideration of other fuel configuration candidates (e.g., 10×10 Boiling Water Reactor assembly).

REFERENCES

1. Blue Ribbon Commission. 2012. "Blue Ribbon Commission on America's Nuclear Future, Report to the Secretary of Energy." Prepared by the Blue Ribbon Commission on America's Nuclear Future for the U.S. Department of Energy, Washington, D.C.
2. DOE - U.S. Department of Energy. 2013. *Strategy for the Management and Disposal of Used Nuclear Fuel and High-Level Radioactive Waste*. U.S. Department of Energy, Washington, D.C.
3. H. ADKINS, K. GEELHOOD, B. KOEPPEL, J. COLEMAN, J. BIGNELL, G. FLORES, J.A. WANG, S. SANBORN, R. SPEARS, and N. KLYMYSHYN, "Used Nuclear Fuel Loading and Structural Performance Under Normal Conditions of Transport – Demonstration of Approach and Results on Used Fuel Performance Characterization", September 30, 2013 FCRD-UFD-2013-000325
4. K. GEELHOOD, H. ADKINS, S. SANBORN, B. KOEPPEL, and N. KLYMYSHYN, "Analytical Model Methodology Development and Demonstration of Approach on Used Fuel Performance Characterization for Condition of Normal Transportation (14568)," *WM2014 Conference,* Phoenix, Arizona, USA, March 2-6, 2014.
5. J. BIGNELL, G. FLORES, and D. AMMERMAN, "Cask Assembly Level Modeling to Determine Used Nuclear Fuel Assembly Loading Environments Resulting From Normal Conditions of Rail Transport (14511)," *WM2014 Conference,* Phoenix, Arizona, USA, March 2-6, 2014.
6. J. COLEMAN, and R. SPEARS, "Detailed PWR Fuel Rod and Grid Finite Element Analysis to Provide Equivalent Rod Stiffness and Damping and Equivalent Grid Shell Thickness to PWR Used Nuclear Fuel (UNF) Assembly (14525)," *WM2014 Conference,* Phoenix, Arizona, USA, March 2-6, 2014.
7. J.A. WANG, H. JIANG, and H. WANG, "The Potential Impact of Interface Bonding Efficiency on High-Burnup Spent Nuclear Fuel Vibration Integrity during Normal Transportation (14502)," *WM2014 Conference,* Phoenix, Arizona, USA, March 2-6, 2014.
8. J.A. WANG and H. WANG, B. BEVARD, and R. HOWARD, "Reversal Bending Fatigue Testing on Zry-4 Surrogate Rod (14503)," *WM2014 Conference,* Phoenix, Arizona, USA, March 2-6, 2014.
9. ASTM E 1049-85. (Reapproved 2005). *Standard practices for cycle counting in fatigue analysis*. ASTM International.
10. DOE (U.S. Department of Energy). 1987. Characteristics of Spent Fuel, High-Level Wastes which May Require Long-Term Isolation. DOE/RW-0184, U.S. Department of Energy, Washington, D.C.
11. C.W. MAYS, "Summary Report of Commercial Reactor Criticality Data for McGuire Unit 1", B00000000-01717-5705-00063 Rev 01, April 13, 1998.

ACKNOWLEDGEMENTS

The authors would like to thank John Wagner and Rob Howard (Oak Ridge National Laboratory) for instilling the concept of evaluating moderate to high burnup fuel under conditions of normal transport. The authors would also like to thank John Orchard, Ned Larson, and the U.S. Department of Energy for providing funding for this initiative.